

Molecular beam epitaxial growth and physical properties of AlN/GaN superlattices with an average 50% Al composition

Siqi Li(李思琦), Pengfei Shao(邵鹏飞), Xiao Liang(梁潇), Songlin Chen(陈松林), Zhenhua Li(李振华), Xujun Su(苏旭军), Tao Tao(陶涛), Zili Xie(谢自力), Bin Liu(刘斌), M. Ajmal Khan, Li Wang, T. T. Lin, Hideki Hirayama, Rong Zhang(张荣), and Ke Wang(王科)

Citation: Chin. Phys. B, 2024, 33 (**12**): 126801. DOI: 10.1088/1674-1056/ad84cc
Journal homepage: http://cpb.iphy.ac.cn; http://iopscience.iop.org/cpb

What follows is a list of articles you may be interested in

A first-principles study on remote van der Waals epitaxy through a graphene monolayer on semiconductor substrates

Rui Hou(侯锐) and Shenyuan Yang(杨身园)
Chin. Phys. B, 2023, 32 (**6**): 066801. DOI: 10.1088/1674-1056/ac92d6

Strain compensated type II superlattices grown by molecular beam epitaxy

Chao Ning(宁超), Tian Yu(于天), Rui-Xuan Sun(孙瑞轩), Shu-Man Liu(刘舒曼), Xiao-Ling Ye(叶小玲), Ning Zhuo(卓宁), Li-Jun Wang(王利军), Jun-Qi Liu(刘俊岐), Jin-Chuan Zhang(张锦川), Shen-Qiang Zhai(翟慎强), and Feng-Qi Liu(刘峰奇)
Chin. Phys. B, 2023, 32 (**4**): 046802. DOI: 10.1088/1674-1056/ac7cd4

Extended phase diagram of $La_{1-x}Ca_xMnO_3$ by interfacial engineering

Kexuan Zhang(张可璇), Lili Qu(屈莉莉), Feng Jin(金锋), Guanyin Gao(高关胤), Enda Hua(华恩达), Zixun Zhang(张子璔), Lingfei Wang(王凌飞), and Wenbin Wu(吴文彬)
Chin. Phys. B, 2021, 30 (**12**): 126802. DOI: 10.1088/1674-1056/ac003e

Temperature effects of GaAs/$Al_{0.45}Ga_{0.55}As$ superlattices on chaotic oscillation

Xiao-Peng Luo(罗晓朋), Yan-Fei Liu(刘延飞), Dong-Dong Yang(杨东东), Cheng Chen(陈诚), Xiu-Jian Li(李修建), and Jie-Pan Ying(应杰攀)
Chin. Phys. B, 2021, 30 (**10**): 106805. DOI: 10.1088/1674-1056/ac04a6

Temperature-dependent subband mobility characteristics in n-doped silicon junctionless nanowire transistor

Ya-Mei Dou(窦亚梅), Wei-Hua Han(韩伟华), Yang-Yan Guo(郭仰岩), Xiao-Song Zhao(赵晓松), Xiao-Di Zhang(张晓迪), Xin-Yu Wu(吴歆宇), Fu-Hua Yang(杨富华)
Chin. Phys. B, 2019, 28 (**6**): 066804. DOI: 10.1088/1674-1056/28/6/066804

Molecular beam epitaxial growth and physical properties of AlN/GaN superlattices with an average 50% Al composition

Siqi Li(李思琦)[1], Pengfei Shao(邵鹏飞)[1], Xiao Liang(梁潇)[1], Songlin Chen(陈松林)[1], Zhenhua Li(李振华)[1,2], Xujun Su(苏旭军)[3], Tao Tao(陶涛)[1], Zili Xie(谢自力)[1], Bin Liu(刘斌)[1], M. Ajmal Khan [4], Li Wang[4], T. T. Lin[4], Hideki Hirayama[4], Rong Zhang(张荣)[1], and Ke Wang(王科)[1,4,†]

[1] *Jiangsu Provincial Key Laboratory of Advanced Photonic and Electronic Materials, School of Electronic Science and Engineering, Nanjing University, Nanjing* 210000, *China*

[2] *School of Opto-Electronic Engineering, Zaozhuang University, Zaozhuang* 277160, *China*

[3] *Suzhou Institute of Nano-Tech and Nano-Bionics, Chinese Academy of Sciences, Suzhou* 215000, *China*

[4] *RIKEN, Saitama, Japan*

(Received 27 July 2024; revised manuscript received 23 September 2024; accepted manuscript online 9 October 2024)

We report molecular beam epitaxial growth and electrical and ultraviolet light emitting properties of (AlN)*m*/(GaN)*n* superlattices (SLs), where *m* and *n* represent the numbers of monolayers. Clear satellite peaks observed in XRD 2θ–ω scans and TEM images evidence the formation of clear periodicity and atomically sharp interfaces. For (AlN)*m*/(GaN)*n* SLs with an average Al composition of 50%, we have obtained an electron density up to 4.48×10^{19} cm^{-3} and a resistivity of 0.002 Ω·cm, and a hole density of 1.83×10^{18} cm^{-3} with a resistivity of 3.722 Ω·cm, both at room temperature. Furthermore, the (AlN)*m*/(GaN)*n* SLs exhibit a blue shift for their photoluminescence peaks, from 403 nm to 318 nm as GaN is reduced from $n = 11$ to $n = 4$ MLs, reaching the challenging UVB wavelength range. The results demonstrate that the (AlN)*m*/(GaN)*n* SLs have the potential to enhance the conductivity and avoid the usual random alloy scattering of the high-Al-composition ternary AlGaN, making them promising functional components in both UVB emitter and AlGaN channel high electron mobility transistor applications.

Keywords: AlGaN, superlattices (SLs), molecular beam epitaxy (MBE)

PACS: 68.65.Cd, 77.55.Px, 81.05.Ea, 74.62.Dh **DOI:** 10.1088/1674-1056/ad84cc

1. Introduction

Wide bandgap AlGaN semiconductors have some excellent properties, such as continuously tunable bandgaps ranging from 3.4 eV (GaN) to 6.2 eV (AlN), high breakdown field, high thermal conductivity, and a high electron saturation velocity. Due to these unique properties, AlGaN has widespread applications in UV emitters and high electron mobility transistors (HEMTs).[1–5]

However, the AlGaN-based UV emitters have been suffering from low efficiency, particularly the UVB LEDs (280 nm–320 nm) that must use AlGaN with Al compositions about 30%–50%, the most difficult for such ternary alloys.[6–8] Compared to UVC emitters, the epitaxial growth of AlGaN UVB emitters on AIN templates is expected to be more challenging due to their higher lattice mismatch.[8,9] Although various methods have been proposed to address the lattice mismatch issues, such as Al-ion implantation,[10] patterned substrates,[11] and superlattices.[12,13] However, the reported efficiencies of UVB LEDs emitting at a wavelength of 300–320 nm remain below 2%. On the other hand, beyond the traditional AlGaN/GaN HEMTs based on the 2DEG at their interface, thanks to the polarization field, AlGaN itself is also a promising channel material for HEMTs. The breakdown voltage of high Al composition $Al_xGa_{1-x}N$ ($x > 0.5$) has been proven to be much higher than that of GaN, and it is expected to be three times that of GaN.[14,15] Therefore, HEMTs based on $Al_yGa_{1-y}N/Al_xGa_{1-x}N$ heterostructures with $x < y$ have been proposed to enhance the breakdown voltage and high-temperature stability.[16–19]

One notable strategy is the replacement of AlGaN random alloys with monolayer (ML) level (AlN)*m*/(GaN)*n* short period superlattices, or digital alloys (DAs), where *m* and *n* represent the numbers of MLs of AlN and GaN, respectively. Such SLs possess the ability to tune the emission wavelength by adjusting the GaN ML number, as first reported in 1993.[20] Since then, many studies have been conducted to further explore this promising material architecture.[21–26] For instance, Gao Na *et al*.[22] have demonstrated the successful growth of high-crystallinity (AlN)*m*/(GaN)*n* DAs with integral ML films and atomically sharp interfaces by MOVPE. Additionally, a few works have studied the potential of using nitride SLs as HEMT channel materials.[27,28] Ada Wille *et al*.[27] have reported that the insertion of AlN/GaN SLs within the AlGaN/GaN structure effectively forms a multi-channel 2DEG, and the structure significantly improves the mobility of HEMTs, which is partly attributed to the reduction of AlGaN random alloy scattering. Furthermore, some groups have reported the SL doping technology in UV LEDs

†Corresponding author. E-mail: kewang@nju.edu.cn

© 2024 Chinese Physical Society and IOP Publishing Ltd

to improve the carrier transport.[21,25,29,30] Jiaming Wang *et al.*[30] have adopted ultrathin $Al_{0.63}GaN_{0.37}/Al_{0.46}Ga_{0.54}N$ short-period SLs with an average Al composition of 51% for efficient Mg doping in a 280 nm DUV-LEDs, achieving a hole density of up to 8.1×10^{18} cm^{-3} at room temperature (RT).

In this study, we have adopted (AlN)*m*/(GaN)*n* SLs as alternatives to AlGaN random alloys to some extent. To verify this, traditional AlGaN random alloys and (AlN)*m*/(GaN)*n* SLs (with an equivalent Al composition of ~0.5 for the SLs) were prepared for comparison, where the ratios $m:n$ are 3:3, 4:4, 6:6, and 11:11 respectively. We have separately investigated the electrical (Si-doped and Mg-doped) and luminescent properties of AlGaN random alloys and SLs. The SLs exhibit significantly superior electrical properties compared to traditional AlGaN random alloys. The results indicate that (AlN)*m*/(GaN)*n* SLs hold promise for enhancing the conductivity of high Al composition AlGaN, which is beneficial for both optical and electronic applications.

2. Experimental methods

The (AlN)*m*/(GaN)*n* SLs were grown on AlN/sapphire templates by a RIBER Compact 21 plasma assisted MBE.[31–35] The MBE techniques are capable of precisely controlling the composition and growth thickness of the epitaxial layer through rapidly switching of sources by shutter opening and closing, thereby facilitating the growth of ultrathin hetero-structures.[33,36–39] In these (AlN)*m*/(GaN)*n* SLs samples, *m* and *n* were 3, 4, 6, and 11 for both AlN and GaN, resulting in an equivalent Al composition of approximately 50%. For comparison, $Al_xGa_{1-x}N$ ($x\sim0.5$) random alloys were also grown. All samples were grown on AlN templates, which were grown by metal–organic chemical vapor deposition (MOCVD) on *c*-plane sapphire substrates. A 500 nm thick Mo layer was deposited on the backside of the AlN templates.[32–34]

Before MBE growth, the AlN templates were solvent cleaned, loaded into the MBE buffer chamber and degassed at 450 °C for 1.5 hours, and then sent to the main growth chamber. During the growth process, AlGaN random alloys and SLs were both grown at 750 °C, monitored by a pyrometer. The nitrogen flow rate was fixed at 0.7 sccm, and the radio frequency power was set to 450 W. The growth rate was 1.7 nm/min, which is beneficial for controlling the ML-level thickness of SLs. The growth process was monitored *in-situ* using reflection high-energy electron diffraction (RHEED). The RHEED pattern and intensity were collected by the KSA400 system equipped with a charge coupled device camera and a frame collector. High-resolution x-ray diffraction (HR-XRD) and transmission electron microscopy (TEM) were used for structural characterization. Atomic force microscopy (AFM) was used to study the surface morphology. The electrical properties were investigated through Hall-effect measurements. The optical properties were investigated through photoluminescence (PL) measurements.

3. Results and discussion

Figure 1 shows the growth process of the (AlN)*m*/(GaN)*n* SLs and the corresponding RHEED intensity variation. One period of the (AlN)*m*/(GaN)*n* SLs growth process is divided into two parts: the growth of AlN and GaN layer. We adopt a proper Al modulation epitaxy (AME) method to grow the AlN layer without Al droplet formation at a lower temperature.[32] The growth of GaN was in a slightly metal-rich environment.[35]

Under Al-rich conditions, excess Al atoms are prone to accumulate and form Al droplets because the reevaporation rate of Al atoms is relatively low at lower temperatures. Therefore, in the later stage of AlN growth, the Al cell shutter is closed for a certain period of time to consume excess Al adsorption atoms with N*. Additionally, this step is advantageous in preventing the incorporation of excess Al into the subsequent GaN growth. The RHEED intensity gradually decreases when opening the Al cell shutter and nitrogen plasma shutter, and during the closing period of the Al cell shutter, it gradually increases with N* treatment and returns to the original intensity.

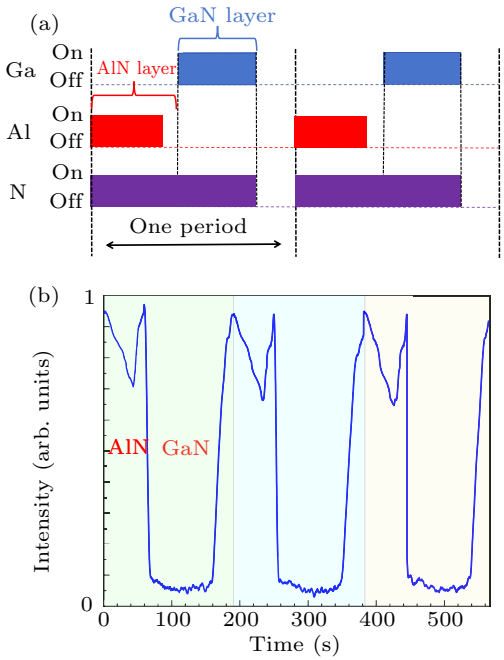


Fig. 1. (a) Schematic diagram of two-period epitaxy of (AlN)*m*/(GaN)*n* SL and (b) the corresponding RHEED intensity variation.

During the growth of the GaN layer, the excess Ga atoms on the sample surface are thermally desorbed due to the high re-evaporation rate of Ga atoms at 750 °C. The RHEED intensity rapidly decreases with the opening of the Ga cell shutter

and nitrogen plasma shutter, quickly reaching and remaining a minimum. Finally, it gradually returns to its original brightest intensity as the thermal desorption time increases. The Si or Mg cell shutter is opened during the growth of AlN and GaN. For 3:3, 4:4, 6:6, and 11:11 SLs, the growth times of both the AlN and GaN layers are 27 s, 36 s, 54 s, and 99 s, respectively.

The surface morphology and roughness of AlGaN random alloys and (AlN)*m*/(GaN)*n* SLs are characterized by AFM images (2×2 μm^2), as shown in Fig. 2. The surfaces of the AlGaN random alloys display numerous hillocks, yet there is no significant difference in surface morphology between undoped and Si-doped samples. However, the Mg-doped AlGaN sample exhibits slightly lower RMS roughness, primarily attributed to the additional epitaxial growth of 15 nm GaN layer on the AlGaN layer to fabricate a lower resistivity p-type ohmic contact. Notably, these hillocks prevalent in the AlGaN random alloys are virtually absent on the surface of the SLs. Furthermore, a notable reduction in the RMS roughness is observed for the SLs compared to the random AlGaN alloys. Figures 2(a′)–2(e′) show the RHEED patterns along the [11–20] azimuth at the end of growth. All RHEED patterns exhibit sharp and well-defined bright streaks, demonstrating the smooth and dry nature of the surfaces.

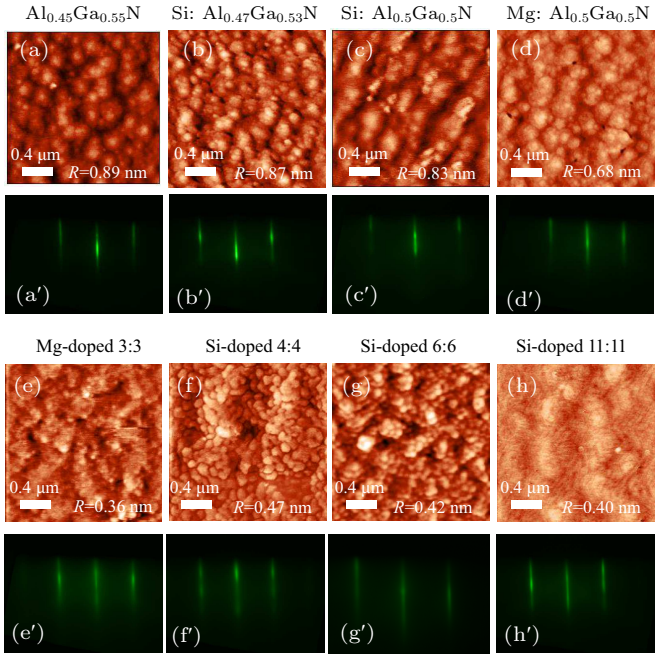


Fig. 2. The 2×2 μm^2 AFM images and RHEED pattern along [11–20] azimuth at the end of growth of AlGaN alloys and (AlN)*m*/(GaN)*n* SLs. (a), (a′) $Al_{0.45}Ga_{0.55}N$, (b), (b′) Si: $Al_{0.47}Ga_{0.53}N$, (c), (c′) Si: $Al_{0.5}Ga_{0.5}N$, (d), (d′) Mg: $Al_{0.5}Ga_{0.5}N$, (e), (e′) Mg: 3:3 SLs, (f), (f′) Si: 4:4 SLs, (g), (g′) Si: 6:6 SLs, (h), (h′) Si: 11:11 SLs.

We have grown four distinct series of (AlN)*m*/(GaN)*n* SLs, specifically designed with thickness ratios of $m:n = 3:3$, 4:4, 6:6, and 11:11 MLs. To confirm the structural parameters of (AlN)*m*/(GaN)*n* SLs, the results of XRD 2θ–ω scans in a very wide range are illustrated in Fig. 3. All samples exhibit a series of satellite peaks across a wide 2θ range from the AlN template and sapphire substrate, demonstrating the formation of sharp interfaces and clearly periodic structures.

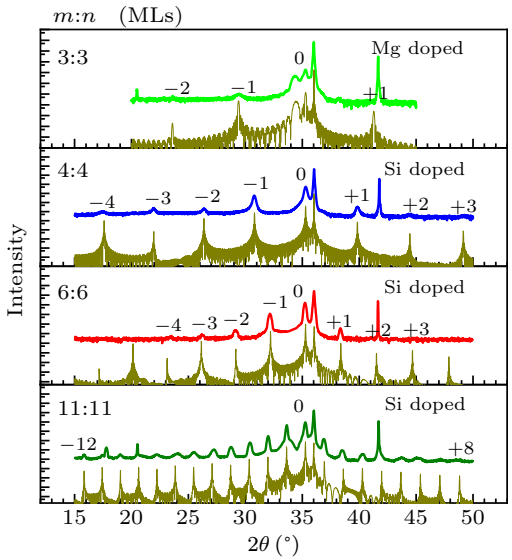


Fig. 3. The HR-XRD patterns of the 2θ–ω (0002) scans of (AlN)*m*/(GaN)*n* SLs. From top to bottom, samples are 3:3, 4:4, 6:6, and 11:11 MLs, respectively. In each panel, the upper line is the measured scan, and the lower line (dark yellow) is the simulated curve.

The satellite peaks are related to the combined thickness of AlN layer and GaN layer. The thickness of each layer and the equivalent Al composition of SLs can be obtained by simulating the satellite peaks and the zero-order equivalent AlGaN peaks simultaneously. For the four (AlN)*m*/(GaN)*n* SLs samples, the simulated thicknesses of AlN and GaN ($m:n$) are 3.1:2.7, 4.0:4.0, 5.8:6.2, and 11.1:11.2 MLs, respectively. These values are in agreement with the growth parameters and the design expectations. The XRD scans reveal that the zero-order satellite positions of the four samples are nearly identical, indicating a similar Al composition in all SLs samples. By simulating the satellite peaks, we can obtain the thicknesses of AlN and GaN, and the Al composition of all samples is approximately 0.5. As the thickness of one period increases, the distance between the satellite peaks decreases. Taking the (AlN)11/(GaN)11 SL as an example, the zero-order peak and the satellite peaks up to 12$^{\text{th}}$ order are clearly observed within a wide angular range of 15°–50°. Notably, the angular interval between the 1st and 2nd order satellite peaks is extremely narrow. For the (AlN)3/(GaN)3 SL, one can see that only the 1$^{\text{st}}$ and 2$^{\text{nd}}$ order satellite peaks are observed and the angular interval between the 1$^{\text{st}}$ and 2$^{\text{nd}}$ order satellite peaks becomes extremely wide.

From the XRD scans of these four series of SLs, the angles of all satellite peaks can be well matched with each other, indicating the excellent repeatability and periodicity of these samples. The $m:n$ and equivalent Al compositions are listed in Table 1, which also summarizes Hall effect experimental data obtained at RT.

Table 1. Summary of the structural and electrical parameters of (AlN)*m*/(GaN)*n* SLs and AlGaN random alloys. The equivalent Al compositions and $m:n$ values of SLs were obtained by simulating the zero-order peak and satellite peaks in 2θ–ω XRD scan. The density, resistivity, and mobility were obtained from RT Hall experiments.

Samples		Structural properties		Electrical properties				
		Al (%)	Simulation ($m:n$)	Si (10^{19} cm^{-3})	Mg (10^{19} cm^{-3})	Density (10^{19} cm^{-3})	Resistivity (Ω·cm)	Mobility (cm^2/(V·s))
Si doped	AlGaN	0.47	–	4		0.95	0.118	5.55
	AlGaN	0.50	–	4		1.52	0.037	9.93
	4:4	0.50	4.0 : 4.0	4		1.9	0.021	15.5
	6:6	0.47	5.8 : 6.2	2		0.74	0.026	31.3
	11:11	0.50	11.1 : 11.2	4		4.48	0.002	64.6
Mg doped	AlGaN	0.50	–		5	–		
	3:3	0.52	3.1 : 2.7		5	0.183	3.722	0.917

As clearly shown in Fig. 4, high-angle annular dark-field scanning transmission electron microscopy (HAADF-STEM) measurements were precisely conducted on the 3:3 and 4:4 SL samples to gain a deeper insight into their microstructural characteristics. In the images, the bright stripes represent GaN, which contrasts sharply with the darker stripes corresponding to AlN. This alternating pattern of GaN and AlN stripes is distinctive of the SL's layered structure.

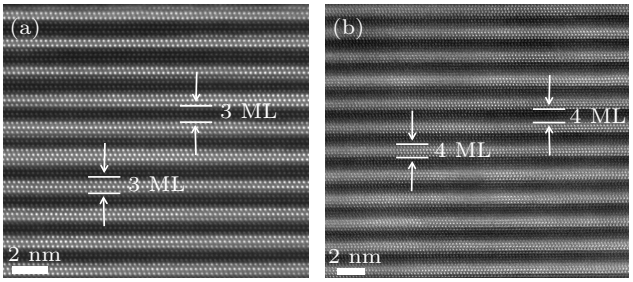


Fig. 4. Cross-sectional HAADF-STEM images of (AlN)*m*/(GaN)*n* SLs. (a) 3:3 SL, (b) 4:4 SL.

The TEM images of the two SL samples clearly demonstrate that each period exhibits remarkable periodicity and a uniform thickness. Furthermore, typical magnified TEM images reveal the exceptional quality of the GaN/AlN interface. In two types of samples, the interfaces appear atomically smooth and sharp, indicating a high crystallinity and minimal defects. This atomic-level smoothness and sharpness are crucial for the SL's performance, as they facilitate efficient charge transport and minimize scattering at the interfaces. However, notable fluctuations in the thickness of the ML layers are observed in both samples. For instance, as shown in Fig. 4(a), within the GaN layer, some localized white stripes exhibit a thickness of 4 MLs, indicating variations in the thickness of these layers.

As shown in Table 1, we have systematically doped conventional AlGaN random alloys and (AlN)*m*/(GaN)*n* SL with Si and Mg in order to investigate the n-type and p-type electrical properties. For Si-doped traditional AlGaN random alloys, the electron mobility values are 5.55 cm^2/(V·s) and 9.93 cm^2/(V·s), corresponding to the electrical resistivities of 0.118 Ω·cm and 0.037 Ω·cm, respectively. The mobility of Si-doped SLs is significantly higher than that of AlGaN random alloys, leading to a correspondingly lower resistivity. For Si-doped SLs, as shown in Fig. 5, we have noticed that the mobility of Si-doped SLs increases with the thickness of one period. As the thickness of one period increases from 8 MLs to 22 MLs, the mobility increases from 15.5 cm^2/(V·s) to 64.6 cm^2/(V·s), exhibiting a linear trend of increase. In the (AlN)11/(GaN)11 SL with a Si concentration of 4×10^{19} cm^{-3}, the highest mobility observed is 64.6 cm^2/(V·s), corresponding to a resistivity of 0.002 Ω·cm. Based on the activation energies calculated through temperature dependent Hall effect results in our previous work,[33] it is evident that Si dopant ionization energies in SLs are much lower than that for usual AlGaN random alloys.

Notably, achieving p-type AlGaN with high Al composition has presented greater challenges compared to n-type one. In this work, to facilitate ohmic contacts, a p-GaN epitaxial layer with a thickness of approximately 15 nm was deposited onto both the AlGaN random alloy and the (AlN)3/(GaN)3 SL. Unfortunately, no conclusive results are obtained from the Hall measurements conducted on Mg-doped $Al_{0.5}Ga_{0.5}N$ random alloy. Conversely, for the Mg-doped (AlN)3/(GaN)3 SL, we have achieved a hole density of 1.83×10^{18} cm^{-3}, a resistivity of 3.722 Ω·cm, and a mobility of 0.917 cm^2/(V·s).

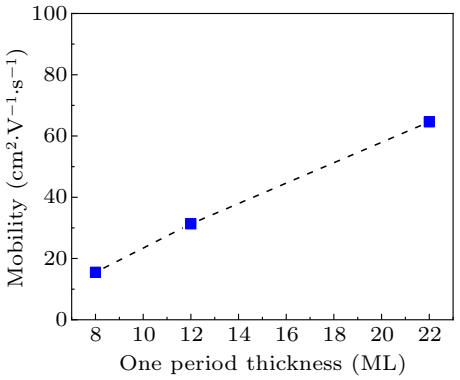


Fig. 5. Relationship between the electron mobility and the thickness of one period in Si-doped (AlN)*m*/(GaN)*n* SL.

The optical properties were studied through PL using a 213 nm laser excitation source, as shown in Fig. 6. For the traditional AlGaN random alloy, the peak wavelength is 293 nm for $Al_{0.47}Ga_{0.53}N$, and 284 nm for $Al_{0.5}Ga_{0.5}N$. However, for

the (AlN)*m*/(GaN)*n* SL with the Al compositions, the spectra differ from the AlGaN random alloys. As the thickness of AlN and GaN increases from 11 MLs → 6 MLs → 4 MLs, the peak wavelength shows a blue shift from 403 nm → 357 nm → 318 nm at RT, reaching the UVB wavelength range. Furthermore, as the GaN layer thickness decreases, a significant enhancement in luminescence intensity is also observed. As the thickness of the GaN well decreases, the quantum confinement effect leads to larger energy separation between the electron and hole subbands, resulting in the blue shift of PL peaks.[33] On the other hand, a narrower GaN well leads to a higher spatial overlap of the the wave functions of electrons and holes,[40] which thus enhances the radiative recombination probability and the luminescence intensity. On the contrary, a wider GaN well results in a reduction in transition energy, and a separation of the wave functions in space due to the tilted strong polarization field, and thus the PL intensity reduces significantly due to the quantum confinement Stark effect (QCSE).

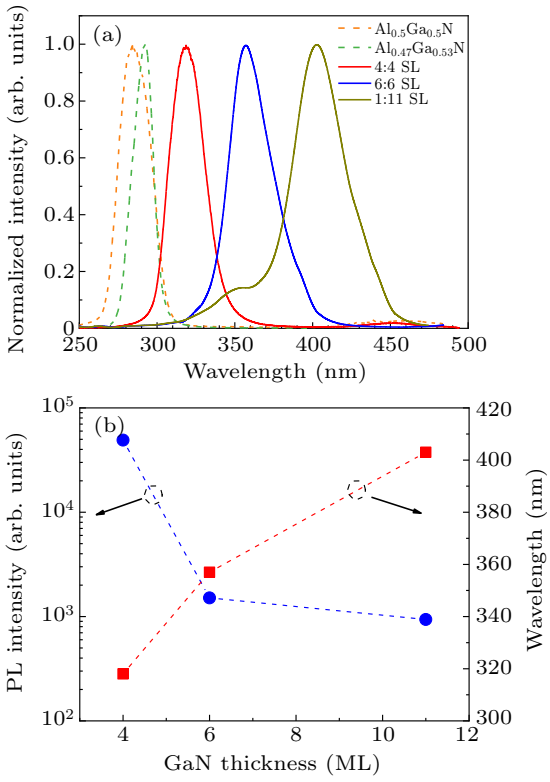


Fig. 6. (a) The normalized PL spectra of AlGaN random alloys and (AlN)*m*/(GaN)*n* SLs. (b) The relationship between the GaN thickness of one period and the intensity and wavelength.

4. Conclusion

In this work, we have successfully grown (AlN)*m*/(GaN)*n* SLs and AlGaN random alloys (with Al compositions of approximately 0.5 for all samples) by PA-MBE, where $m:n$ are 3:3, 4:4, 6:6, and 11:11 MLs. XRD scans and TEM images indicate the formation of sharp interfaces and distinct periodic structures, demonstrating excellent periodicity of the SLs. Notably, the hole or electron mobilities in the Mg or Si doped (AlN)*m*/(GaN)*n* SLs were significantly higher than those traditional AlGaN random alloys grown under identical conditions in the same MBE system. Moreover, within the (AlN)*m*/(GaN)*n* SLs, a blue shift towards the UVB wavelength range was observed, accompanied by an enhanced luminescence intensity, as the GaN thickness decreased within one period. These results demonstrate the potential of (AlN)*m*/(GaN)*n* SLs as functionally viable alternatives in electronic and optical device applications.

Acknowledgements

Project supported by the National Key R&D Program of China (Grant No. 2022YFB3605600), the National Natural Science Foundation of China (Grant No. 61974065), the Key R&D Project of Jiangsu Province, China (Grant Nos. BE2020004-3 and BE2021026), Postdoctoral Fellowship Program of CPSF (Grant No. GZC20231098), the Jiangsu Special Professorship, Collaborative Innovation Center of Solid State Lighting and Energy-saving Electronics.

References

[1] Kneissl M, Seong T Y, Han J and Amano H 2019 *Nat. Photon.* **13** 233
[2] Kneissl M and Rass J 2016 *Springer Series in Material Science* (Vol. 227) (Switzerland: Springer International Publishing) pp. 115–215
[3] Arulkumaran S, Vicknesh S, Ng G, Liu Z H, Bryan M and Lee C H 2010 *Electrochem. Solid-State Lett.* **13** H169
[4] Xie J, Mita S, Bryan Z, Guo W, Hussey L, Moody B, Schlesser R, Kirste R, Gerhold M, Collazo R and Sitar Z 2013 *Appl. Phys. Lett.* **102** 171102
[5] Lachab M, Sun W, Jain R, Dobrinsky A, Gaevski M, Rumyantsev S, Shur M and Shatalov M 2017 *Appl. Phys. Express* **10** 012702
[6] Khan M A, Yamada Y and Hirayama H 2024 *Phys. Status Solidi A* **13** 2300581
[7] Khan M A, Itokazu Y, Maeda N, Jo M, Yamada Y and Hirayama H 2020 *ACS Appl. Electron. Mater.* **2** 1892
[8] Fischer A J, Allerman A A, Crawford M H, Bogart K H A, Lee S R, Kaplar R J, Chow W W, Kurtz S R, Fullmer K W and Figiel J J 2004 *Appl. Phys. Lett.* **84** 3394
[9] Bryan I, Bryan Z, Mita S, Rice A, Hussey L, Shelton C, Tweedie J, Maria J, Collazo R and Sitar Z 2016 *J. Cryst. Growth.* **451** 65
[10] Tao H C, Xu S R, Zhang J C, Su H K, Gao Y, Zhang Y C, Zhou H and Hao Y 2023 *Opt. Express* **13** 20850
[11] Tanaka S, Teramura S, Shimokawa M, Yamada K, Omori T, Iwayama S, Sato K, Miyake H, Iwaya M, Takeuchi T, Kamiyama S and Akasaki I 2021 *Appl. Phys. Express* **14** 055505
[12] Kamarundzaman A, Bakar A S, Azman A, Omar A Z, Talik N A, Supangat A and Abd Majid W H 2021 *Sci. Rep.* **11** 9724
[13] Stanchu H V, Kuchuk A V, Lytvyn P M, Mazur Y I, Maidaniuk Y, Benamara M, Li S B, Kryvyi S, Kladko V P, Belyaev A E, Wang Zh M and Salamo G J 2018 *Mater. Des.* **157** 141
[14] NanjoT, Takeuchi M, Suita M, Oishi T, Abe Y, Tokuda Y and Aoyagi Y 2008 *Appl. Phys. Lett.* **92** 263502
[15] Coltrin M E, Baca A G and Kaplar R J 2017 *ECS J. Solid State Sci. Technol.* **6** S3114
[16] MaedaR, Ueno K, Kobayashi A and Fujioka H 2022 *Appl. Phys. Express* **15** 031002
[17] Baca A G, Klein B A, Wendt J R, Lepkowski S M, Nordquist C D, Armstrong A M, Allerman A A, Douglas E A and Kaplar R J 2019 *IEEE Electron Device Lett.* **40** 17
[18] Singhal J, Chaudhuri R, Hickman A, Protasenko V, Xing H G and Jena D 2022 *APL Mater.* **10** 111120

[19] Khachariya D, Mita S, Reddy P, Dangi S, Dycus J H, Bagheri P, Breckenridge M H, Sengupta R, Rathkanthiwar S, Kirste R, Kohn E, Sitar Z, Collazo R and Pavlidis S 2022 *Appl. Phys. Lett.* **120** 172106

[20] Khan M A, Kuznia J N, Olson D T, George T and Pike W T 1993 *Appl. Phys. Lett.* **63** 3470

[21] Islam S M, Protasenko V, Lee K, Rouvimov S, Verma J, Xing H and Jena D 2017 *Appl. Phys. Lett.* **111** 091104

[22] Gao N, Feng X, Lu S Q, Lin W, Zhuang Q Q, Chen H Y, Huang K, Li S P and Kang J Y 2019 *Cryst. Growth Des.* **19** 1720

[23] Jmerik V, Toropov A, Davydov V and Ivanov S 2021 *Phys Status Solidi Rapid Res. Lett.* **15** 2100242

[24] Sun W, Tan C K and Tansu N 2017 *Sci. Rep.* **7** 11826

[25] Nikishin S A, Holtz M and Temkin H 2005 *Jpn. J. Appl. Phys.* **44** 7221

[26] Kipshidze G, Kuryatkov V, Zhu K, Borisov B, Holtz M, Nikishin S and Temkin H 2003 *J. Appl. Phys.* **93** 1363

[27] Wille A, Yacoub H, Debald A, Kalisch H and Vescan A 2015 *J. Electron.* **44** 1263

[28] Itakura H, Nomura T, Arita N, Okada N, Wetzel C M, Chow T P and Tadatomo K 2020 *AIP Advances* **10** 025133

[29] Nikishin S A 2018 *Appl. Sci.* **8** 2362

[30] Wang J M, Wang M X, Xu F J, Liu B Y, Lang J, Zhang N, Kang X N, Qin Z X, Yang X L, Wang X Q, Ge W K and Shen B 2022 *Light Sci. Appl.* **11** 71

[31] Shao P F, Fan X, Li S Q, Chen S L, Zhou H, Liu H, Guo H, Xu W. Z, Tao T, Xie Z L, Lu H, Wang K, Liu B, Chen D J, Zheng Y D and Zhang R 2023 *Appl. Phys. Lett.* **122** 142102

[32] Shao P F, Li S Q, Zhou H, Li Z H, Zhang D Q, Tao T, Yan Y, Xie Z L, Wang K, Liu B, Chen D J, Zheng Y D, Zhang R, Lin T, Wang L and Hirayama H 2022 *J. Phys. D: Appl. Phys.* **55** 364002

[33] Li S Q, Liang X, Shao P F, Chen S L, Li Z H, Su X J, Tao T, Xie Z L, Khan M A, Wang L, Lin T T, Hirayama H, Liu B, Chen D J, Wang K and Zhang R 2024 *Appl. Phys. Lett.* **125** 112102

[34] Li Z H, Shao P F, Wu Y Z, Shi G J, Tao T, Xie Z L, Chen P, Zhou Y G, Xiu X Q, Chen D J, Liu B, Wang K, Zheng Y D, Zhang R, Lin T, Wang L and Hirayama H 2021 *Jpn. J. Appl. Phys.* **60** 075504

[35] Li Z H, Shao P F, Shi G J, Wu Y Z, Wang Z P, Li S Q, Zhang D Q, Tao T, Xu Q J, Xie Z L, Ye J D, Chen D J, Liu B, Wang K, Zheng Y D and Zhang R 2022 *Chin. Phys. B* **31** 018102

[36] Smorchkova I P, Haus E, Heying B, Kozodoy P, Fini P, Ibbetson J P, Keller S, DenBaars S P, Speck J S and Mishra U K 2000 *Appl. Phys. Lett.* **76** 718

[37] Kim K C, Schmidt M C, Sato H, Wu F, Fellows N, Saito M, Fujito K, Speck J S, Nakamura S and DenBaars S P 2007 *Phys. Stat. Sol. (RRL)* **1** 125

[38] Ivanov S V, Nechaev D V, Sitnikova A A, Ratnikov V V, Yagovkina M A, Rzheutskii N V, Lutsenko E V and Jmerik V N 2014 *Semicond. Sci. Technol.* **29** 084008

[39] Zhang H P, Xue J S, Fu Y R, Yang M, Zhang Y C, Duan X L, Qiang W T, Li L X, Sun Z P, Ma X H, Zhang J C and Hao Y 2020 *J. Cryst. Growth.* **535** 125539

[40] Sun W, Tan C K and Tansu N 2017 *Sci. Rep.* **7** 6671